Polymer Composites

WILEY | spe INSPIRING PLASTICS PROFESSIONALS

RESEARCH ARTICLE

Flow-Induced Microstructure Manipulation for Thermal-Humid Performance Enhancement in Quantum Dots Luminescent Composite

Xuan Yang[1] | Tianxu Zhang[1] | Changcong Wang[2] | Linyi Xiang[1] | Bin Xie[3] | Xiaobing Luo[1]

[1]School of Energy and Power Engineering, Huazhong University of Science and Technology, Wuhan, China | [2]Shaanxi Coal Chemical Industry Technology Research Institute Co., Ltd, Xi'an, China | [3]School of Mechanical Science and Engineering, Huazhong University of Science and Technology, Wuhan, China

Correspondence: Bin Xie (binxie@hust.edu.cn) | Xiaobing Luo (luoxb@hust.edu.cn)

Received: 27 May 2025 | **Revised:** 12 November 2025 | **Accepted:** 29 November 2025

Keywords: filler orientation | heat dissipation | light-emitting device | moisture resistance | quantum dots

ABSTRACT

Quantum dots (QDs) are widely used in optoelectronic devices due to their excellent optical properties. However, their photoluminescent characteristics are highly sensitive to temperature and humidity, impacting the performance and reliability of QD-based devices. Traditional strategies typically address either heat dissipation or moisture resistance but fail to handle both high temperature and humidity simultaneously. To improve thermal-humid stability, we proposed integrating horizontally oriented hexagonal boron nitride (hBN) microstructures into QDs composites. This design enhances in-plane thermal conductivity and reduces through-plane water vapor diffusivity, as confirmed by effective medium theory. We developed a flow-induced method using fluid shear force during spin coating to achieve the horizontal alignment of hBN. The fabricated transmissive white light laser diodes (WLDs), termed LC/HhBN WLDs, demonstrated superior optical and thermal performance. Under a driving current of 500 mA, LC/HhBN with 5 wt% hBN exhibited a maximum surface temperature 54°C lower than conventional LC WLDs. Additionally, the luminous efficiency of LC/HhBN was 131.34 lm W^{-1}, surpassing LC's 124.76 lm W^{-1}. In a 600-h aging test at 60°C and 90% relative humidity, QDs-silicone/HhBN with 5 wt% hBN retained 82% of its initial light intensity, compared to only 65% for QDs-silicone.

1 | Introduction

Quantum dots (QDs) are widely utilized in optoelectronic applications as an indispensable color-converting component, owing to their remarkable optical properties including high luminous efficiency, broad absorption spectra, and size-tunable emission spectra [1, 2]. Nevertheless, their performance is highly vulnerable to environmental factors, particularly temperature and humidity. Both elevated temperature and hydro-oxidative corrosion in humid conditions introduce defect states within QDs [3]. These defect states enhance non-radiative recombination pathways, leading to degradation of luminous efficiency and operating lifetime, and even thermal quenching at excessively high temperatures [4, 5]. During the light conversion process, QDs absorb and emit light while simultaneously generating heat via non-radiative relaxation [6]. The silicone matrix, which is commonly used to encapsulate QDs, exhibits an inherently low thermal conductivity of approximately 0.15 W m^{-1} K^{-1}, significantly hindering heat dissipation. This results in thermal accumulation, further elevating the operational temperature of QDs [7]. In humid environments, the loosely structured polymer matrix allows water and oxygen molecules to penetrate easily, causing

Highlights

- Spin coating could effectively realize hBN's horizontal orientation.
- Under 5 wt% of horizontally oriented hBN, the composite's thermal conductivity was tripled.
- Under 5 wt% of horizontally oriented hBN, the composite's water vapor diffusivity was halved.
- At 500 mA, device working temperature was reduced by 54°C.
- After 600-h aging test, the light intensity was improved by 26.2%.

damage to the QDs. Under the combined stress of high temperature and humidity, the performance and reliability of QDs-based optoelectronic devices face severe limitations.

To mitigate the challenges posed by temperature and humidity, researchers have explored various strategies [8]. For enhancing heat dissipation, incorporating high thermal-conductive fillers into the composite stands out as the most effective and widely adopted approach [9–11]. Hexagonal boron nitride (hBN), owing to its exceptional in-plane thermal conductivity of approximately 600 $W m^{-1} K^{-1}$ and minimal light absorption, has emerged as a preferred material for improving heat dissipation in luminescent composites (LCs) [12, 13]. To improve the heat transfer efficiency between QDs and the incorporated hBN platelets, techniques such as electrostatic bonding have been developed to strengthen their interaction, which reduced the working temperature by 22.7°C [14, 15]. Moreover, leveraging the anisotropic thermal conductivity of hBN, advanced methods like ice-template-directed alignment and air-bubble-assisted assembly have been proposed to construct three-dimensional thermal dissipation networks in the matrix, significantly boosting the composite's thermal conductivity [16, 17]. However, most of these studies primarily focus on thermal issues, with limited consideration of the moisture stability. For improving stability in humid environments, moisture-resistant packaging strategies have been devised [18]. These include the application of protective buffer layers such as silica [19, 20], superior hydrophobic silica coating [21], the development of densely packaging matrix like silica glass [22, 23] and poly(styrene-ethylene-butylene-styrene) [24], and the moisture-resistant packaging architectures like layered packaging [25] and diffusion plate with impermeable flake [26, 27] all of which offer effective protection for QDs. While these methods effectively improve humidity resistance, they often compromise heat dissipation due to the low thermal conductivity of the added barrier layers. The existing strategies often overlook the combined impact of heat and humidity in real-world applications. Consequently, there is a pressing need to develop an integrated heat- and moisture- management packaging solution for QDs converted devices to address these dual challenges effectively.

HBN is a promising material to address the dual challenges of heat and moisture management in QDs composites, owing to its exceptional in-plane thermal conductivity and moisture impermeability [18, 28]. Given the anisotropic thermal and structural properties of hBN, its orientation plays a pivotal role in determining performance outcomes. In this work, we proposed a microstructure featuring horizontally oriented hBN within QDs composites to simultaneously enhance the heat dissipation and moisture resistance. Effective medium theory (EMT) was employed to calculate the thermal conductivity and water vapor diffusivity (WAD) of composites with both randomly and horizontally oriented hBN, while the finite element method (FEM) was utilized to analyze heat and moisture transport, elucidating the underlying mechanisms. Our findings highlight the superior thermal-humid performance achieved with horizontal orientation. To achieve this alignment microstructure, we implemented a flow-induced orientation strategy. Shear forces within fluid flow have been demonstrated to achieve particle orientation [29]. By utilizing centrifugal forces during spin coating, we effectively orient hBN platelets horizontally within the QDs LC. This configuration yielded a composite with enhanced in-plane thermal conductivity and reduced moisture diffusivity, which were demonstrated by experimental thermal conductivity and WAD test respectively. Leveraging this approach, we fabricated QDs converted white laser diodes (LC/HhBN WLDs) which outperformed traditional QDs LC WLDs in optical, thermal, and humid-environment stability.

2 | Material and Methods

2.1 | Materials

Red-emissive CdSe/ZnS QDs with a peak wavelength of 630 nm were provided by Poly Opto-Electronics, Shenzhen, China. Yellow-emissive phosphor with a peak wavelength of 538 nm was provided by Intematix, Fremont, USA. hBN platelets with an average diameter of 45 μm were purchased from Momentive, Indiana, USA. Two-component silicone (SYLGARD 184, $A{:}B = 10{:}1$) was purchased from Dowsil, Midland, USA.

2.2 | Fabrication of Silicone With Horizontally Oriented hBN (Silicone/HhBN)

The fabrication process of silicone/HhBN was shown in Figure 1a. First, hBN platelets (with mass fractions of 5 wt% and 10 wt%) were uniformly mixed with 4 g silicone gel and degassed to prepare the hybrid fluid. Subsequently, 0.2 g hybrid fluid was dropped onto the center of the spinning sapphire substrate (with a diameter of 25 mm) by using an injector, and then underwent a 5-s spin coating process under 2000 rpm to form a uniform film on the substrate. The spin-coating parameters used in this work were adopted from our previous study, in which we systematically investigated the influence of the parameters on the orientation of hBN platelets in polymer fluid [30]. Then, the substrate was heated at 100°C for 2 min to cure the film. Finally, on the cured film, the aforementioned spinning-coating processes were repeated to fabricate a 9-layer silicone/HhBN composite with a thickness of 1 mm and a diameter of 25 mm. As a comparison, silicone with randomly oriented hBN (silicone/RhBN) was also prepared. Silicone and hBN of different mass fractions were well mixed and vacuumed. Then, the mixture was poured into an aluminum alloy mold (with a diameter of 12.7 mm and thickness of 1 mm) and cured at 100°C for 15 min.

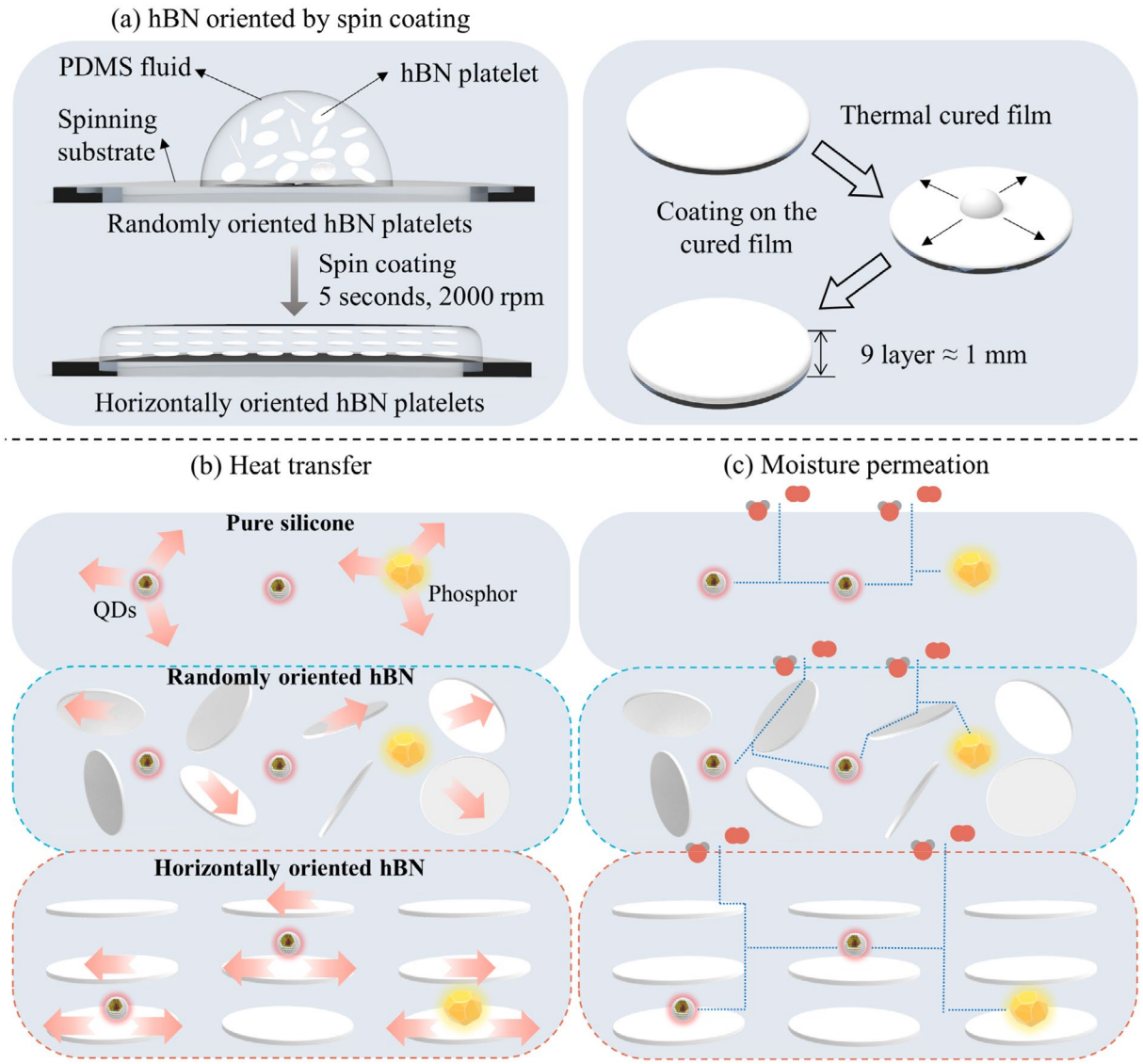

FIGURE 1 | Schematic showing the QDs composite embedded with hBN platelets. (a) Spin coating and layer-by-layer curing process of horizontally oriented hBN platelets. Schematic of (b) heat transfer and (c) moisture permeation in LC, LC/RhBN, and LC/HhBN.

2.3 | Fabrication of LC/hBN

The fabrication process of LC/HhBN was similar to that of the silicone/HhBN composite. First, 4 g silicone gel, 0.8 g phosphor, 240 μL QDs-chloroform solution and hBN (with mass fraction of 5 and 10 wt%) were uniformly mixed and degassed. The following repeated spinning-coating steps are similar to those in the fabrication of silicone/HhBN, while the curing temperature is changed to 85°C. As a reference, LC was also prepared. Two gram-silicone gel, 0.4 g phosphor, and 120 μL QDs-chloroform solution were uniformly mixed, degassed and then poured into an aluminum alloy mold (with a diameter of 25 mm and thickness of 1 mm). Finally, it was cured at 85°C (to reduce temperature-induced degradation) for 15 min.

2.4 | Characterizations

Scanning electron microscope (SEM) and energy dispersive spectroscopy (EDS) mapping images of QDs-silicone/HhBN composite were obtained by a field-emission SEM (RISE-CLARA, TESCAN, Brno, The Czech Republic). Samples were coated with a thin layer of gold prior to testing by a broad argon ion beam system (PECSII685, GATAN, Pleasanton, USA) with 300 s. The ultraviolet–visible (UV–VIS) absorption spectra of QDs-silicone and QDs-silicone with randomly and horizontally oriented hBN (QDs-silicone/RhBN and QDs-silicone/HhBN) were measured by a UV–VIS spectrophotometer (SolidSpec-3700, Shimadzu, Kyoto, Japan). The thermal diffusivity α of silicone, silicone/RhBN and silicone/HhBN were tested by a laser flash analysis (LFA457, Netzsch, Selb, Germany). Density ρ of the samples was tested by an electron density meter (XF-220SD, LICHEN, Shanghai, China). Specific heat capacity C_p of the samples was measured by a differential scanning calorimetry (Diamond DSC, PerkinElmer, Shanghai, China). Thermal conductivity κ of the samples was calculated by $\kappa = \alpha \cdot \rho \cdot C_p$. The photoluminescence (PL) spectra and time resolved PL (TRPL) were obtained by a fluorescence spectrofluorometer (EI FLS980, Edinburgh Instruments, Livingston, UK) at a pulse excitation wavelength of 450 nm.

Surface temperature distributions of QDs-LC and QDs-LC/HhBN were obtained by a thermal infrared imager (SC620, FLIR, Wilsonville, USA). Optical performances were tested by an integrating sphere system (ATA-1000, Everfine, Hangzhou, China). The samples were excited by a commercial laser diode (L450P1600MM, Thorlabs, Newton, USA). WAD of the samples was carried out by fitting the water vapor absorption curves with Fick diffusion [31, 32]:

$$M_t / M_\infty = 1 - \frac{8}{\pi} \sum_{n=0}^{n=\infty} \frac{1}{(2n+1)^2} e^{-D(2n+1)^2 \pi^2 \frac{t}{l^2}} \quad (1)$$

where M_t is the total mass of the samples at time t. M_∞ is the total mass of the sample saturated with water vapor. D is the water vapor diffusivity, and l is the thickness of the sample. The water vapor absorption experiments were proceeded under 20°C and 70% RH through a Dynamic Vapor Sorption (IGAsorp, Hiden, Warrington, UK).

2.5 | Analytical Model

EMT [33] model was used to study the thermal conductivity and WAD of the composite with horizontally and randomly oriented particles, respectively.

For in-plane thermal conductivity:

$$\kappa_{\text{in-plane}} = \kappa_{\text{matrix}} \frac{2 + V_f\left[\beta_{11}(1-L_{11})(1+<\cos^2\theta>) + \beta_{33}(1-L_{33})(1-<\cos^2\theta>)\right]}{2 - V_f\left[\beta_{11}L_{11}(1+<\cos^2\theta>) + \beta_{33}L_{33}(1-<\cos^2\theta>)\right]} \quad (2)$$

where κ_{matrix} is the thermal conductivity of the polymer matrix (0.15 $\text{W m}^{-1}\text{K}^{-1}$ for silicone) and V_f is the volume fraction of the filler. L_{11} and L_{33} are the geometric factors dependent on the particle, which are listed in Table 1. β_{11} and β_{33} are the factors related to thermal conductivities of filler and matrix, which are listed in Table 1. $<\cos^2\theta>$ is 1/3 and 1 for randomly oriented and horizontally oriented composites, respectively.

WAD of the silicone containing hBN could also be calculated by the EMT model:

$$D_{\text{through-plane}} = D_{\text{matrix}} \frac{1 + V_f\left[\beta_{11}(1-L_{11})(1-<\cos^2\theta>) + \beta_{33}(1-L_{33})<\cos^2\theta>\right]}{1 - V_f\left[\beta_{11}L_{11}(1-<\cos^2\theta>) + \beta_{33}L_{33}<\cos^2\theta>\right]} \quad (3)$$

where D_{matrix} is the WAD of the polymer matrix ($2.86\times10^{-9}\,\text{m}^2\,\text{s}^{-1}$ for silicone). The related parameters for calculation are listed in Table 1.

3 | Results and Discussion

Figure 1b provides a schematic of heat dissipation in LC, LC/RhBN and LC/HhBN composites. In the light-emitting process, QDs and phosphor absorb blue light and convert it to red and yellow light, with heat generated from the non-radiative process. In pure silicone, the low thermal conductivity leads to heat accumulation and elevated temperatures, compromising device performance. The incorporation of hBN markedly improves heat dissipation. Owing to the anisotropic thermal-conductive feature of hBN, its orientation critically influences the direction of heat flux. In LC/RhBN composite, where hBN is randomly oriented, the heat flux is disordered, whereas in LC/HhBN, with horizontally oriented hBN, the heat flux is transferred orderly along the horizontal plane, facilitating more efficient heat dissipation. This leverages hBN's high in-plane thermal conductivity to rapidly transfer heat away from luminescent particles. Figure 1c depicts the moisture permeation process within a hBN-incorporated polymer. Driven by pressure and concentration differences, water and oxygen molecules infiltrate the silicone and diffuse through it. The impermeable nature of hBN extends the diffusion pathway, effectively mitigating moisture-induced degradation of the luminescent particles. The thermal conductivity of the filler-matrix system containing anisotropic fillers can be predicted by Equation (2). Under hBN volume fraction of 4.7 vol% (mass fraction of 10 wt%), $\kappa_{\text{in-plane}}$ is calculated as 0.45 $\text{W m}^{-1}\text{K}^{-1}$ for randomly oriented-hBN composite and 0.60 $\text{W m}^{-1}\text{K}^{-1}$ for horizontally oriented-hBN composite, which are 3 times and 4 times that of silicone, respectively. Considering interfacial thermal resistance $R_b = 0$, 10^{-6}, and $10^{-4}\,\text{m}^2\,\text{K W}^{-1}$, the thermal conductivity was calculated and listed in Table 2. At $R_b = 10^{-4}\,\text{m}^2\,\text{K W}^{-1}$, it has a great influence on the thermal conductivity of the composites. The calculated WADs are 1.85×10^{-9} and $1.13\times10^{-9}\,\text{m}^2\,\text{s}^{-1}$ for silicone with randomly and

TABLE 1 | Parameters for calculation of EMT model.

	V_f (m_f)/%	κ_{matrix} or D_{matrix}	β_{11}	β_{33}	L_{11}	L_{33}	$<\cos^2\theta>$
Thermal conductivity	4.7 (10)	0.15 $\text{W m}^{-1}\text{K}^{-1}$	60.98	1.03	0.02	0.97	1/3, 1
Water vapor diffusivity	4.7 (10)	$2.86\times10^{-9}\,\text{m}^2\,\text{s}^{-1}$	−1.02	−30.96	0.02	0.97	1/3, 1

TABLE 2 | Calculated thermal conductivity $\kappa_{\text{in-plane}}$ by EMT model under different R_b.

	$R_b = 0\,\text{m}^2\,\text{K W}^{-1}$	$R_b = 10^{-6}\,\text{m}^2\,\text{K W}^{-1}$	$R_b = 10^{-5}\,\text{m}^2\,\text{K W}^{-1}$
Randomly	0.45	0.42	0.29
Horizontally	0.60	0.55	0.36

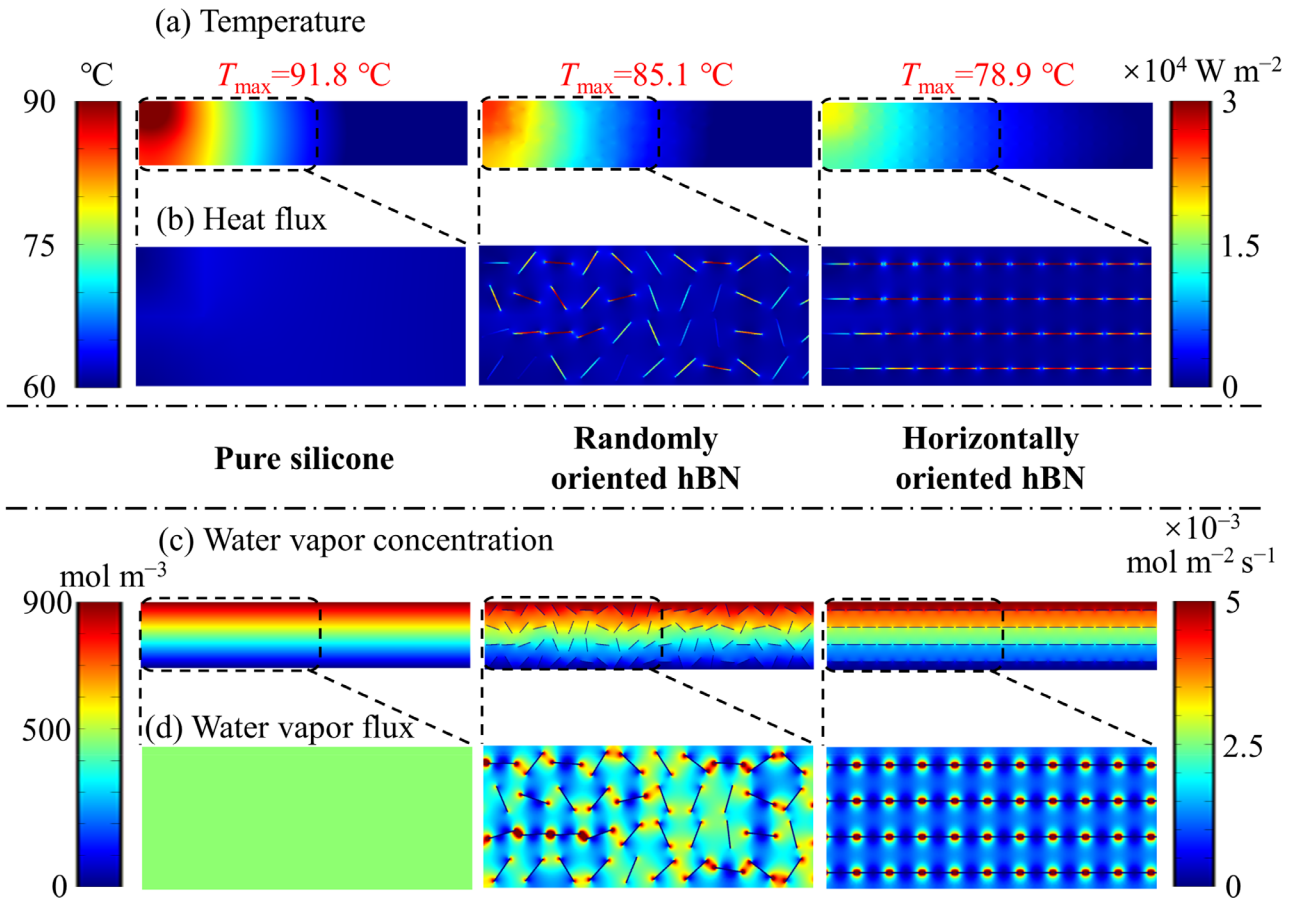

FIGURE 2 | Finite element method analysis. (a) Temperature distributions, (b) heat flux distributions, (c) water vapor concentration distributions, and (d) water vapor flux distributions of pure silicone, silicone/RhBN, and silicone/HhBN.

horizontally oriented hBN respectively, which are lower than 2.86×10^{-9} of pure silicone. The above analysis and calculation by EMT model indicate that hBN can improve the in-plane thermal-conductive and through-plane moisture-resistance performance of silicone, and horizontal orientation of hBN can further improve these capabilities.

A two-dimensional FEM was utilized to investigate the mechanism of heat transfer enhancement and moisture resistance of silicone/HhBN composite. Figure 2a,b illustrates the temperature and heat flux distributions, respectively. A 5 W heat source, with a length of 1 mm and height of 0.5 mm, was positioned at the internal upper center of a composite sample (length of 10 mm and height of 1 mm). All surfaces were configured for natural convection heat transfer as $5\,W\,m^{-2}\,K^{-1}$ at an ambient temperature of 20°C. It is found that among those composites, the silicone/HhBN composite exhibited the lowest maximum temperature of 78.9°C, compared to 91.8°C for pure silicone, which recorded the highest. Heat flux distributions in Figure 2b elucidate the underlying mechanism. The heat flux in the silicone matrix was about $2000\,W\,m^{-2}$, while that could exceed $30{,}000\,W\,m^{-2}$ in hBN due to the high thermal conductivity. In contrast to silicone/RhBN, where the disordered orientation of hBN led to less efficient heat dissipation, the orderly horizontal alignment in the silicone/HhBN composite facilitated more effective heat transfer along the temperature gradient. Consequently, the majority of hBN platelets in the silicone/HhBN composite exhibited elevated heat flux, resulting in a reduced overall temperature. Figure 2c,d present the water vapor concentration and flux distributions, respectively. Constant water vapor concentrations of 900 and $0\,mol\,m^{-3}$ were set on the top and bottom boundary, respectively. The side boundary and the hBN boundaries were set as impermeable. Due to this concentration difference, water vapor within the composites displayed a graded distribution. As shown in Figure 2d, the water vapor flux in pure silicone showed a uniform value of $2.57\times10^{-3}\,mol\,m^{-2}\,s^{-1}$. The presence of impermeable hBN altered the flux patterns in both silicone/RhBN and silicone/HhBN composites, effectively suppressing water vapor diffusion. In most regions of these composites, the flux was lower than that in pure silicone, with localized increases to $5\times10^{-3}\,mol\,m^{-2}\,s^{-1}$ occurring only in narrow gaps between hBN platelets. The horizontal orientation of hBN maximized the impermeable area along the primary diffusion direction thereby increasing the diffusion path length, leading to a more pronounced reduction in water vapor flux compared to the randomly oriented hBN in the silicone/RhBN composite. This dual enhancement in thermal and moisture management underscores the efficacy of the horizontally oriented hBN microstructure.

Figure 3a presents the fabricated samples of silicone, silicone/HhBN, and silicone/RhBN composites. Figure 3b compares the thermal conductivities of the samples, demonstrating a significant enhancement upon hBN incorporation. The horizontally

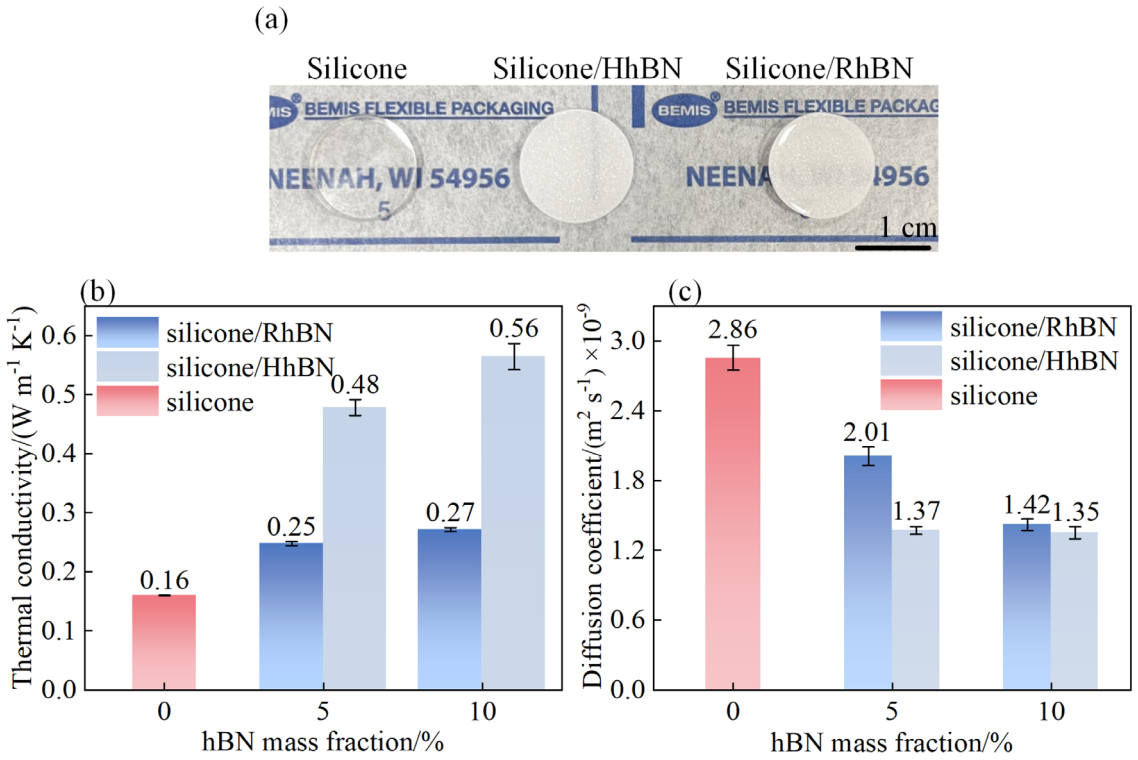

FIGURE 3 | Testing of silicone, silicone/RhBN, and silicone/HhBN of 5 wt% and 10 wt% hBN contents. (a) Photographs; (b) thermal conductivity; (c) WAD.

orientated hBN proved more effective in-plane thermal conductivities of 0.48 and 0.56 $W m^{-1} K^{-1}$ at 5 wt% and 10 wt% hBN, respectively, which are nearly double the values of 0.25 and 0.27 $W m^{-1} K^{-1}$ for silicone/RhBN composites at the same hBN loadings. Compared to other current strategies, our work showed superiority in thermal conductivity enhancement. In Xie's work [17], they built a 3D-interconnected hBN network within the composite and realized a thermal conductivity of 0.37 $W m^{-1} K^{-1}$ under hBN loading of 4.5 wt%. The thermal conductivity enhancement per 1 wt% was 33.19%. In our work, this value was 44%, which is 10.81% higher than that of Xie's work. Figure 3c examines the WAD, measured as through-plane diffusivity $D_{\text{through-plane}}$ due to the samples' thin, circular film geometry with a large diameter-to-thickness ratio. Pure silicone exhibited a WAD of $2.86 \times 10^{-9} m^2 s^{-1}$, which decreased to $2.01 \times 10^{-9} m^2 s^{-1}$ in silicone/RhBN composite and $1.37 \times 10^{-9} m^2 s^{-1}$ in silicone/HhBN composite at 5 wt% of hBN, and $1.42 \times 10^{-9} m^2 s^{-1}$ and $1.35 \times 10^{-9} m^2 s^{-1}$ at 10 wt% of hBN. These tested WADs agreed with the theoretical predictions, reflecting hBN's impermeability and the resulting extended diffusion pathways. These results confirm hBN's ability to enhance both heat dissipation and moisture resistance in polymer composites, with horizontal orientation via spin coating markedly improving thermal conductivity and moisture resistance compared to random orientation. Figure 4 explores hBN's impact on the optical properties of QDs. Figure 4a compares the UV–VIS absorption spectra of QDs-silicone, QDs-silicone/RhBN, and QDs-silicone/HhBN composites. The absorption spectra reveal that QDs exhibit broad absorption across the UV–VIS range, with stronger absorption in the UV region. Comparing the spectra of different samples, it can be found that the addition and orientation of hBN slightly influenced the absorption characteristic of QDs. Figure 4b displays the relative PL spectra, where QDs in all samples exhibited a narrow PL spectrum with a peak wavelength of 630 nm and a full-width-at-half-maximum of 32 nm. In addition, PL lifetime $\tau 1$ of QDs was measured to study their luminous stability in different composites. Figure 4c shows the TRPL decay curves, which were well fitted by an exponential function $I(t) = A_1 e^{-t/\tau 1} + A_2 e^{-t/\tau 2}$, where $I(t)$ is the PL initial intensity at time t. The PL lifetime of QDs in silicone, silicone with randomly and horizontally oriented hBN was 15.25 ns, 14.91 ns, and 15.97 ns, respectively. Compared to the referenced QDs-silicone, the PL lifetime variations of QDs-silicone/RhBN and QDs-silicone/HhBN were −2.2% and 4.7%, respectively. These findings indicate that neither the incorporation nor the orientation of hBN significantly alters the luminous stability of QDs, preserving their optical performance across the tested composites.

Figure 5a illustrates the operational schematic of transmissive WLDs. A blue laser diode emits a collimated laser beam that strikes the geometric center of the LC, where QDs and phosphor partially convert the blue light into red and yellow light, respectively. This converted light mixes with residual blue light to produce white light. The centralized nature of the collimated blue light concentrates both the light conversion and heat generation at the composite's center, resulting in a peak temperature at this location, as depicted in the temperature distribution of Figure 5a. Under these conditions, the high in-plane thermal conductivity of LC/HhBN composite proves more effective in mitigating this centralized thermal load, lowering the operational temperature compared to other composites. Additionally, WAD is significantly influenced by temperature, as elevated temperatures enhance molecular

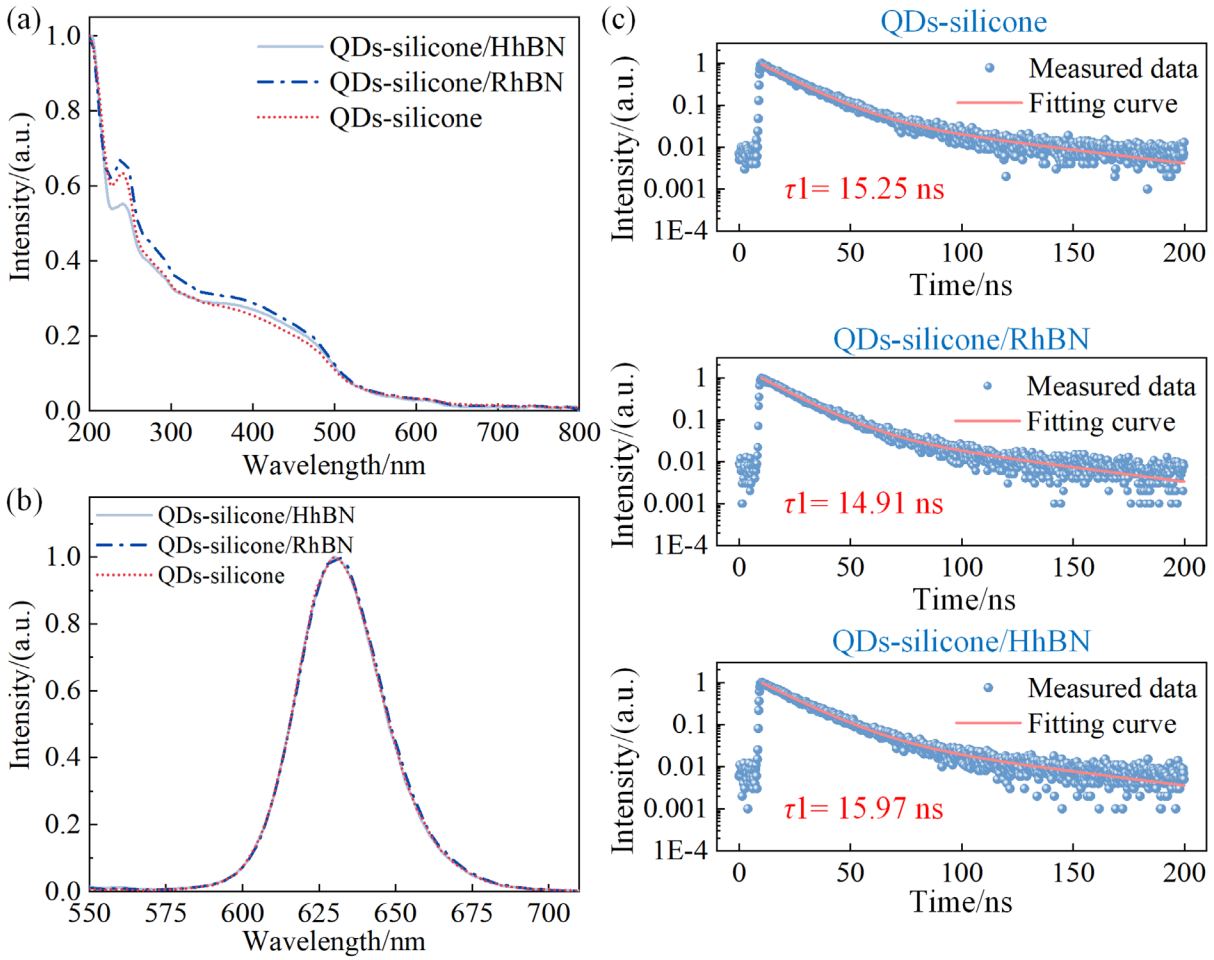

FIGURE 4 | Optical properties of QDs-silicone, QDs-silicone/HhBN, and QDs-silicone/hBN composites. (a) UV–VIS absorption spectra; (b) PL spectra; (c) TRPL decay curves and the calculated lifetime.

motion. Figure 5b displays the fabricated LC and LC/HhBN composites under daylight and UV light, highlighting their visual properties. Figure 5c–e present the SEM images of the vertical section of LC/HhBN composite. The vertical cutting during sample preparation caused the loss of phosphor and hBN particles, leaving cavities in the matrix, with slit-like cavities specifically attributed to hBN platelets. In contrast, Figure 5f shows an SEM image of the horizontal section, where most particles remain intact. The QDs, with their 10 nm size, are too small to be resolved in these images. In the vertical section images, most of the hBN appeared as side and tended to be horizontal, while in the horizontal section image, they appeared as the top surface, demonstrating the horizontal orientation of hBN in LC/HhBN composite. In the vertical section images (Figure 5c–e), hBN platelets predominantly exhibited their thin side facets, while in the horizontal section image (Figure 5f), they were viewed top-down, confirming their horizontal orientation within LC/HhBN composite. Figure 5f further reveals that the interconnected, horizontally oriented hBN platelets form thermal pathways around the phosphor particles, enhancing heat dissipation and reducing operational temperatures effectively. This structural arrangement underscores the efficacy of the horizontal hBN orientation in optimizing the thermal management of transmissive WLDs. Figure 5g illustrates the EDS mapping of N, Y, and Cd elements, which are represented for hBN, phosphor, and QDs, demonstrating a uniform distribution, respectively.

Figure 6 shows the thermal performance of LC and LC/HhBN converted WLDs, which was evaluated using an infrared thermal imager with a surface emissivity of 0.98, as depicted in Figure 6a. The surface temperature distributions were captured once the maximum temperature varied within 1% over 3 min. Figure 6b displays the maximum surface temperatures across a range of driving currents, revealing a consistent increase in temperature with increasing driving current for all samples. However, owing to its superior thermal conductivity, LC/HhBN consistently exhibited lower maximum surface temperatures than LC at each current level, with the temperature difference becoming more pronounced at higher currents. Figure 6c–e shows the temperature distributions of LC, LC/HhBN 5 wt% and LC/HhBN 10 wt% under driving currents of 300, 400 and 500 mA. The infrared images confirm that the maximum surface temperature occurs at the geometric center of the composites, a consequence of the collimated laser beam's central incidence. The horizontal orientation of hBN in LC/HhBN proved highly effective, as the in-plane thermal pathways formed by hBN platelets significantly alleviate the centralized heat accumulation observed in LC. Specifically, at 300 mA, the maximum surface temperatures were 103°C for LC, 73.1°C for LC/HhBN 5 wt%, and 64.4°C for LC/HhBN 10 wt%, yielding

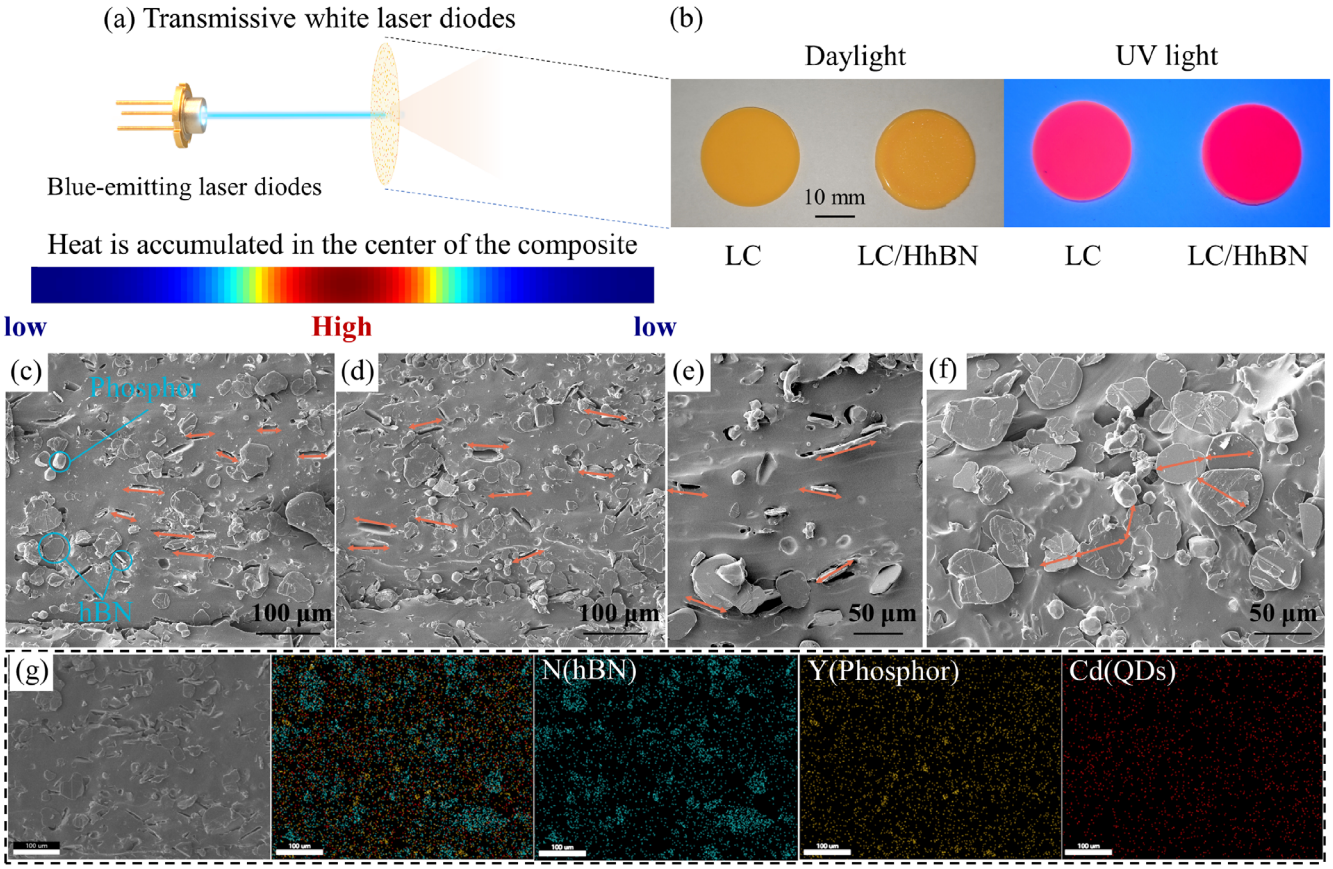

FIGURE 5 | Microstructures of LC/HhBN composite. (a) Operational schematic of transmissive laser diodes and temperature distribution of the illuminated composite; (b) Photographs of LC and LC/HhBN composites under daylight and UV light; (c–e) SEM images of vertical section of LC/HhBN composite; (f) SEM images of horizontal section of LC/HhBN composite. (g) SEM images and the corresponding EDS mapping images of N, Y, and Cd.

temperature reductions of 29.9°C and 38.6°C, respectively. At 500 mA, these values escalated to 225°C, 171°C, and 141°C, respectively, with reductions increasing to 54°C and 84°C. This comparison underscores the exceptional thermal management capability of LC/HhBN, particularly with higher hBN loading, which could enhance optical performance by maintaining lower operating temperatures.

Figure 7 highlights the optical performances of LC and LC/HhBN converted WLDs, with inset showing the device in operation. The lower operating temperatures of LC/HhBN contribute to its superior optical characteristics. In Figure 7a, the LE of LC/HhBN 5 wt% surpasses that of LC across all driving currents, and shows a slower decline tendency. Conversely, LC/HhBN 10 wt% exhibits lower LE at smaller currents, which is mainly attributed to the enhanced light loss caused by the improved scattering effect under higher hBN loading [34, 35]. At 5 wt%, the light loss caused by the hBN scattering effect is weaker than the light enhancement through temperature reduction, while at 10 wt%, the light loss is stronger. At low currents, the generated heat was limited, and thus the thermal performance improvement provided by hBN did not significantly benefit device performance. In contrast, enhanced light loss from hBN particles was dominated, resulting in a lower LE. At 500 mA, the LE values were 131.34 lm W^{-1} for LC/HhBN 5 wt%, 129.65 lm W^{-1} for LC/HhBN 10 wt% and 124.76 lm W^{-1} for LC. As driving current rose, the LE of LC/HhBN 10 wt% approached that of the 5 wt% variant and exceeded LC. Figure 7b shows the correlated color temperature (CCT) of the WLDs, where LC/HhBN demonstrated greater stability with increasing currents. At 500 mA, all tested WLDs maintained a CCT around 4500 K, indicating a neutral white light. The color rendering index (CRI), which measures color accuracy, is presented in Figure 7c. CRI decreased with rising currents due to temperature effects, but LC/HhBN 5 wt% consistently outperformed LC. The LC/HhBN 10 wt% remained more stable, though its CRI was lower between 200 and 400 mA. Over the range of 200 mA to 700 mA, CRI values shifted from 82.7 to 75.4 for LC/HhBN 5 wt%, 81.2 to 74.6 for LC, and 77.9 to 77.3 for LC/HhBN 10 wt%. Figure 7d compares the emission spectra of the tested WLDs at 500 mA, revealing similar power distributions across the samples. However, LC/HhBN 5 wt% exhibited a stronger yellow and red intensity, accounting for its higher LE and CRI, and slightly lower CCT. Collectively, these results demonstrated that LC/HhBN, particularly at 5 wt%, achieved the best optical performance by optimizing temperature reduction and minimizing light loss among the tested configurations.

Furtherly, a temperature-humidity-control aging experiment was proceeded to investigate the humidity stability of QDs in silicone with horizontally oriented hBN. Figure 8a presents photographs of the tested samples, while Figure 8b depicts the intensity aging curves for QDs-silicone, QDs-silicone/HhBN

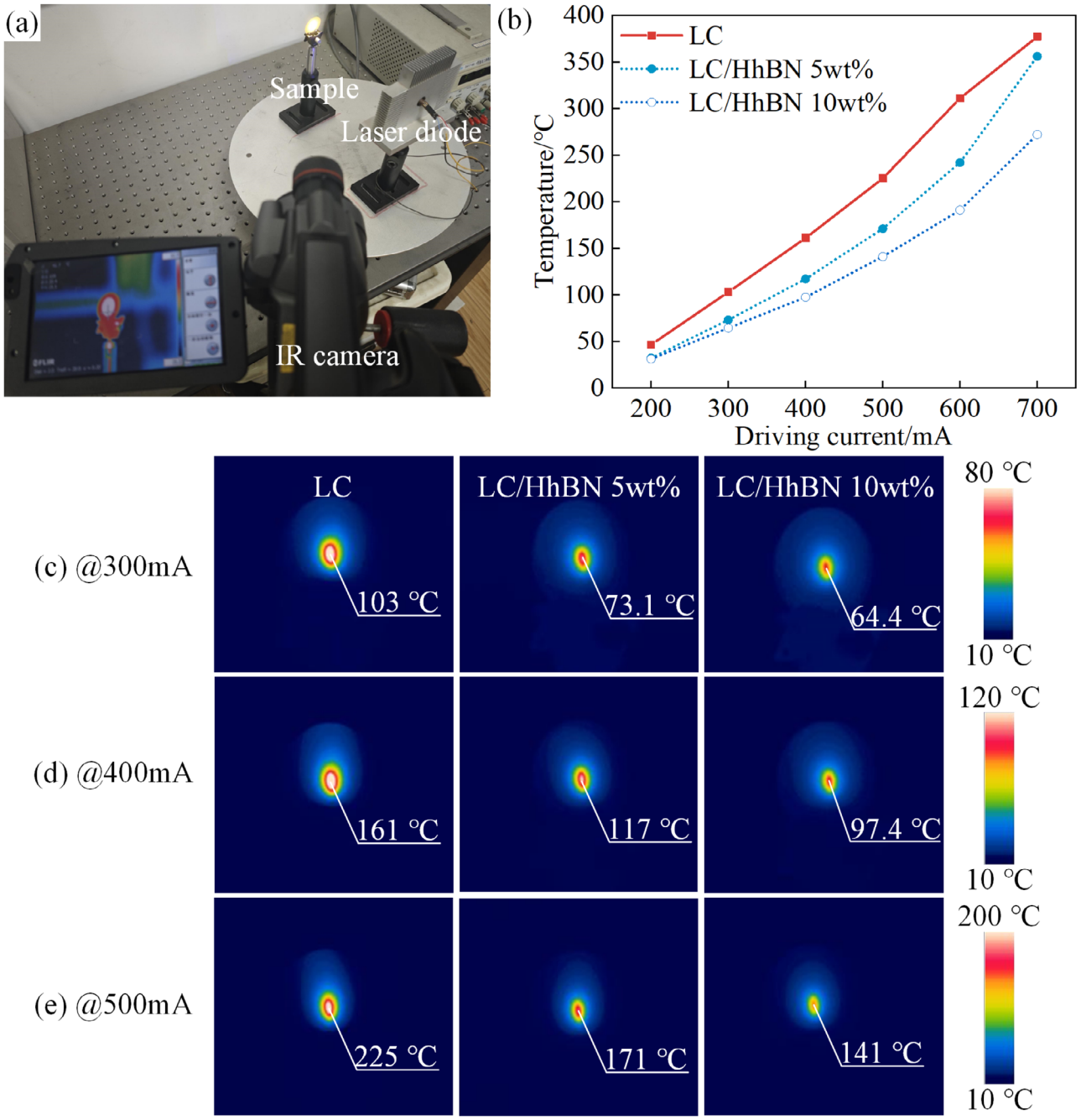

FIGURE 6 | Thermal performance comparison of LC and LC/HhBN WLDs. (a) Temperature measurement set up; (b) maximum surface temperature curves of the tested samples under different driving currents; Surface temperature distributions of the tested samples under (c) 300 mA, (d) 400 mA, and (e) 500 mA.

5 wt%, and QDs-silicone/HhBN 10 wt% composites under conditions of 60°C and 90% relative humidity over 600 h. During the aging process, both decrease and increase stages of intensity were observed, which were caused by the temperature and moisture induced defect states and the water/oxygen molecules induced defect states passivation [21, 22]. After 600 h, the relative intensity of the samples remained 0.82 of QDs-silicone/HhBN 5 wt%, 0.81 of QDs-silicone/HhBN 10 wt%, and 0.65 of QDs-silicone. The time-evolving relative intensity of QDs-silicone and QDs-silicone/HhBN 5 wt% exhibited similar trends. Due to the moisture-resistance horizontally oriented hBN, the decrease in the intensity of QDs-silicone/HhBN was smaller than QDs-silicone. Notably, between 240 and 312 h, the relative intensity of QDs-silicone decreased from 0.87 to 0.70, while that of QDs-silicone/HhBN was 0.92 to 0.86. The time-evolving trend of QDs-silicone/HhBN 10 wt% was completely different from the others. Its intensity sharply dropped from 1.00 to 0.76 in the first 24 h and then slightly increased to 0.87 at 24–312 h, finally decreasing to 0.81 at 312–600 h, which showed a more stable trend in the aging process. This pattern suggests greater long-term stability, likely due to the higher hBN loading enhancing the barrier effect against moisture ingress. These results affirmed that horizontally oriented hBN significantly bolsters the humidity stability of QDs under challenging conditions.

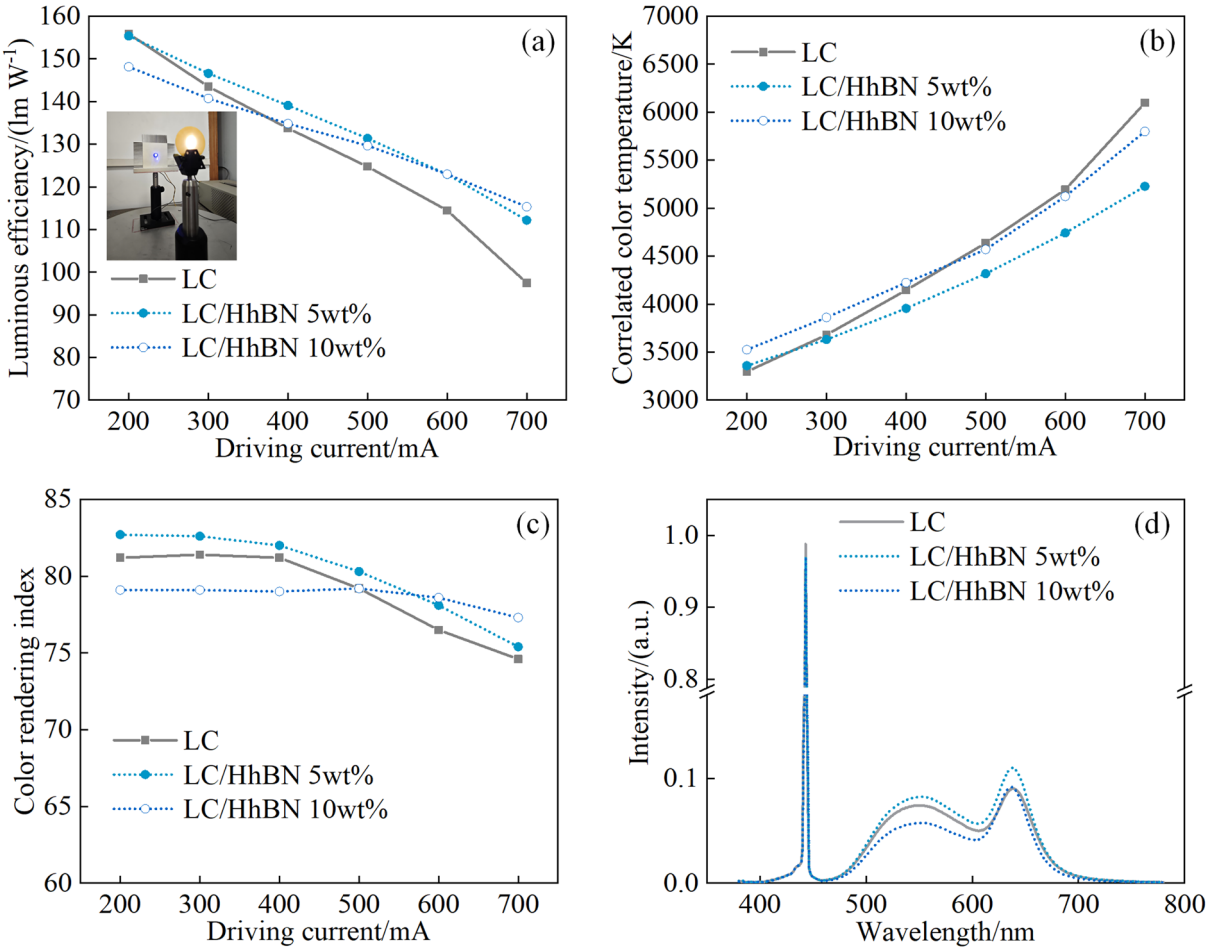

FIGURE 7 | Optical performances comparison of LC and LC/HhBN converted WLDs: (a) LE. Inset is the photograph of the operating WLDs; (b) CCT, and (c) CRI, of the WLDs; (d) spectra of the WLDs under driving current of 500 mA.

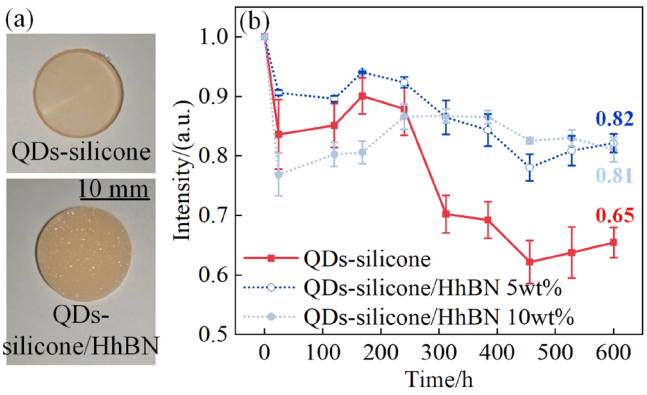

FIGURE 8 | Temperature-humidity-control aging experiment. (a) Photographs of QDs-silicone and QDs-silicone/HhBN composites; (b) normalized intensity aging curves of QDs-silicone, QDs-silicone/HhBN 5 wt% and 10 wt% under 60°C and 90% RH for 600 h.

4 | Conclusion

In this work, we developed a microstructure in composites with horizontally oriented hBN to simultaneously improve the thermal and humidity performance of QDs converted optoelectronic devices. The use of EMT effectively validates the design, demonstrating that silicone/HhBN composite achieved a higher in-plane thermal conductivity and lower through-plane water vapor diffusivity compared to silicone/RhBN composite and pure silicone. The FEM simulation further elucidates the mechanisms: the orderly horizontal hBN orientation boosts heat flux along the temperature gradient for superior heat transfer while forming a larger impermeable area in the diffusion direction to enhance moisture resistance. The experimental results align well with these findings. The tested in-plane thermal conductivity and through-plane WAD of silicone/HhBN composite were significantly higher than pure silicone, respectively. In practical application, the fabricated LC/HhBN 5 wt% WLDs outperform traditional LC WLDs across optical, thermal, and humidity metrics. Additionally, it achieved an excellent CRI and CCT of high-quality white lighting. An aging experiment under 60°C and 90% relative humidity was carried out to further demonstrate the humidity resilience of QDs-silicone/HhBN. These results collectively highlight the robustness of the strategy, offering a promising pathway to elevate the performance and reliability of QDs-based optoelectronic devices in demanding thermal and humid environments.

Author Contributions

Xuan Yang: conceptualization, investigation, writing – original draft, methodology, writing – review and editing, formal analysis, software,

data curation. **Tianxu Zhang:** investigation, validation, methodology, data curation, resources. **Changcong Wang:** investigation, validation, formal analysis, data curation. **Linyi Xiang:** investigation, writing – review and editing, formal analysis, methodology. **Bin Xie:** funding acquisition, project administration, writing – review and editing, supervision. **Xiaobing Luo:** conceptualization, funding acquisition, writing – review and editing, project administration.

Acknowledgments

This work is supported by the Natural Science Foundation of Hubei Province (2024AFB618) and the National Natural Science Foundation of China (52106089).

Funding

This work was supported by the National Natural Science Foundation of China (52106089) and Natural Science Foundation of Hubei Province (2024AFB618).

Conflicts of Interest

The authors declare no conflicts of interest.

Data Availability Statement

The data that support the findings of this study are available from the corresponding author upon reasonable request.

References

1. Q. Wu, F. Cao, W. Yu, et al., "Homogeneous ZnSeTeS Quantum Dots for Efficient and Stable Pure-Blue LEDs," *Nature* 639 (2025): 633–638, https://doi.org/10.1038/s41586-025-08645-4.

2. X. Li, S. Aftab, M. Mukhtar, et al., "Exploring Nanoscale Perovskite Materials for Next-Generation Photodetectors: A Comprehensive Review and Future Directions," *Nano-Micro Letters* 17, no. 1 (2024): 28, https://doi.org/10.1007/s40820-024-01501-6.

3. H. Moon, C. Lee, W. Lee, J. Kim, and H. Chae, "Stability of Quantum Dots, Quantum Dot Films, and Quantum Dot Light-Emitting Diodes for Display Applications," *Advanced Materials* 31, no. 34 (2019): 1804294, https://doi.org/10.1002/adma.201804294.

4. Y. Zhao, C. Riemersma, F. Pietra, R. Koole, C. Donega, and A. Meijerink, "High-Temperature Luminescence Quenching of Colloidal Quantum Dots," *ACS Nano* 6, no. 10 (2012): 9058–9067.

5. H. Liu, G. Jin, J. Wang, et al., "Quantum Dots Mediated Crystallization Enhancement in Two-Step Processed Perovskite Solar Cells," *Nano-Micro Letters* 17, no. 1 (2025): 169, https://doi.org/10.1007/s40820-025-01677-5.

6. Y. Liu, C. Dong, C. Peng, T. Zhang, and L. Zhang, "Nitrogen-Doped Carbon Quantum Dots Enable Efficient Photothermal Conversion for Direct Absorption Solar Collectors," *Solar Energy Materials & Solar Cells* 278 (2024): 113178, https://doi.org/10.1016/j.solmat.2024.113178.

7. H. Li, X. Zhu, D. Zhang, et al., "Thermal Management Towards Ultra-Bright and Stable Perovskite Nanocrystal-Based Pure Red Light-Emitting Diodes," *Nature Communications* 15, no. 1 (2024): 6561, https://doi.org/10.1038/s41467-024-50634-0.

8. T. Zhang, X. Yang, B. Xie, and X. Luo, "Inorganic Ligand Capped Quantum Dot Light-Emitting Diodes: Status and Perspective," *Nanotechnology* 36, no. 10 (2025): 102001, https://doi.org/10.1088/1361-6528/ada2f1.

9. B. Xie, W. Zhao, X. Luo, and R. Hu, "Alignment Engineering in Thermal Materials," *Materials Science & Engineering R: Reports* 154 (2023): 100738, https://doi.org/10.1016/j.mser.2023.100738.

10. X. Yang, X. Zhang, T. Zhang, L. Xiang, B. Xie, and X. Luo, "Paving Continuous Heat Dissipation Pathways for Quantum Dots in Polymer With Orange-Inspired Radially Aligned UHMWPE Fibers," *Opto-Electronic Advances* 7, no. 7 (2024): 240036, https://doi.org/10.29026/oea.2024.240036.

11. Q. Liu, W. Xu, X. Li, et al., "Electrically-Driven Ultrafast Out-Of-Equilibrium Light Emission From Hot Electrons in Suspended Graphene/hBN Heterostructures," *International Journal of Extreme Manufacturing* 6, no. 1 (2023): 015501, https://doi.org/10.1088/2631-7990/acfbc2.

12. X. Yang, S. Zhou, B. Xie, et al., "Enhancing Heat Dissipation of Quantum Dots in High-Power White LEDs by Thermally Conductive Composites Annular Fins," *IEEE Electron Device Letters* 42, no. 8 (2021): 1204–1207, https://doi.org/10.1109/led.2021.3088280.

13. J. D. Caldwell, I. Aharonovich, G. Cassabois, J. H. Edgar, B. Gil, and D. N. Basov, "Photonics With Hexagonal Boron Nitride," *Nature Reviews Materials* 4, no. 8 (2019): 552–567, https://doi.org/10.1038/s41578-019-0124-1.

14. B. Xie, H. Liu, R. Hu, et al., "Targeting Cooling for Quantum Dots in White QDs-LEDs by Hexagonal Boron Nitride Platelets With Electrostatic Bonding," *Advanced Functional Materials* 28, no. 30 (2018): 1801407, https://doi.org/10.1002/adfm.201801407.

15. L. He, L. Yang, C. Ge, R. Liu, W. Li, and X. Zhang, "In-Situ Embedding of Carbon Dots in Boron Nitride for Enhancing Phosphor Stability and Fluorescent Film Heat Dissipation," *Journal of Alloys and Compounds* 968 (2023): 172269, https://doi.org/10.1016/j.jallcom.2023.172269.

16. S. Zhou, Y. Ma, X. Zhang, et al., "White-Light-Emitting Diodes From Directional Heat-Conducting Hexagonal Boron Nitride Quantum Dots," *ACS Applied Nano Materials* 3, no. 1 (2019): 814–819, https://doi.org/10.1021/acsanm.9b02321.

17. B. Xie, Y. Wang, H. Liu, et al., "Targeting Cooling for Quantum Dots by 57.3°C With Air-Bubbles-Assembled Three-Dimensional Hexagonal Boron Nitride Heat Dissipation Networks," *Chemical Engineering Journal* 427 (2022): 130958, https://doi.org/10.1016/j.cej.2021.130958.

18. X. Yang, B. Xie, and X. Luo, "Resisting Oxygen/Moisture Permeation in Quantum Dots Converted Optoelectronic Devices," *Journal of Physics D: Applied Physics* 57, no. 48 (2024): 483001, https://doi.org/10.1088/1361-6463/ad759d.

19. T. Gong, T. Xuan, W. Bai, H. Dong, K. Huang, and R. J. Xie, "Quantum Dot Luminescence Microspheres Enable Ultra-Efficient and Bright Micro-LEDs," *Advanced Materials* 37, no. 9 (2025): 2411999, https://doi.org/10.1002/adma.202411999.

20. F. Ma, X. Meng, S. Li, et al., "Mesoporous Silica-Encapsulated CsPbBr3 Quantum Dots for the Preparation of Green Fiber by Electrospinning," *Optical Materials* 160 (2025): 116744, https://doi.org/10.1016/j.optmat.2025.116744.

21. S. Zhou, B. Xie, X. Yang, X. Zhang, and X. Luo, "Superior Hydrophobic Silica-Coated Quantum Dot for Stable Optical Performance in Humid Environments," *Nanotechnology* 33, no. 19 (2022): 195202, https://doi.org/10.1088/1361-6528/ac4f81.

22. X. Yang, S. Zhou, X. Zhang, L. Xiang, B. Xie, and X. Luo, "Enhancing Oxygen/Moisture Resistance of Quantum Dots by Short-Chain, Densely Cross-Linked Silica Glass Network," *Nanotechnology* 33, no. 46 (2022): 465202, https://doi.org/10.1088/1361-6528/ac86de.

23. Y. H. Kim, H. Lee, S. M. Kang, and B. S. Bae, "Two-Step-Enhanced Stability of Quantum Dots via Silica and Siloxane Encapsulation for the Long-Term Operation of Light-Emitting Diodes," *ACS Applied Materials & Interfaces* 11, no. 25 (2019): 22801–22808, https://doi.org/10.1021/acsami.9b06987.

24. S. N. Raja, Y. Bekenstein, M. A. Koc, et al., "Encapsulation of Perovskite Nanocrystals Into Macroscale Polymer Matrices: Enhanced

Stability and Polarization," *ACS Applied Materials & Interfaces* 8, no. 51 (2016): 35523–35533, https://doi.org/10.1021/acsami.6b09443.

25. N. Pei, X. Yu, S. Zhou, R. Hu, and X. Luo, "Experimental Investigation on the Moisture Stability of QDs-LEDs With Layered Packaging Structure," *IEEE Photonics Technology Letters* 32, no. 22 (2020): 1423–1426, https://doi.org/10.1109/lpt.2020.3029622.

26. F. Yang, B. Li, Y. Li, et al., "One-Step Fast Fabrication of Multi-Layer Quantum Dot Diffusion Plate for Stable Display and Ultra-Long Life, a Novel Quantum Dot Packaging Strategy," *Chemical Engineering Journal* 481 (2024): 148386, https://doi.org/10.1016/j.cej.2023.148386.

27. H. Ji, D. Ye, H. Xu, E. Chen, and Z. Ge, "Multi-Layer Co-Extruded Quantum-Dot Diffuser Plate for Ultra-Large TV Backlights," *Optical Materials Express* 12, no. 4 (2022): 1648–1656, https://doi.org/10.1364/ome.453502.

28. M. Li, G. Huang, X. Chen, et al., "Perspectives on Environmental Applications of Hexagonal Boron Nitride Nanomaterials," *Nano Today* 44 (2022): 101486, https://doi.org/10.1016/j.nantod.2022.101486.

29. X. Zhang, X. Yang, Y. Fan, R. Hu, B. Xie, and X. Luo, "3D-Programmable Streamline Guided Orientation in Composite Materials for Targeted Heat Dissipation," *International Journal of Extreme Manufacturing* 7, no. 2 (2024): 025504, https://doi.org/10.1088/2631-7990/ad92cb.

30. X. Yang, X. Zhang, T. Zhang, L. Xiang, B. Xie, and X. Luo, "Modeling and Optimization of Thermal Interface Materials Featuring Horizontally Oriented Fillers by Flow-Field Driven Strategy," *Composites Part A: Applied Science and Manufacturing* 198 (2025): 109157, https://doi.org/10.1016/j.compositesa.2025.109157.

31. A. Dadaniya and N. V. Datla, "Multilayer Backsheet Characterization Using Diffusion Experiments and Optimization Method for Water Diffusion Simulation Inside the Photovoltaic Module," *IEEE Journal of Photovoltaics* 10, no. 1 (2020): 306–314, https://doi.org/10.1109/jphotov.2019.2953400.

32. J. Crank, *The Mathematics of Diffusion* (Oxford University Press, 1975).

33. C.-W. Nan, R. Birringer, D. R. Clarke, and H. Gleiter, "Effective Thermal Conductivity of Particulate Composites With Interfacial Thermal Resistance," *Journal of Applied Physics* 81, no. 10 (1997): 6692–6699, https://doi.org/10.1063/1.365209.

34. S. Zhou, B. Xie, Y. Ma, W. Lan, and X. Luo, "Effects of Hexagonal Boron Nitride Sheets on the Optothermal Performances of Quantum Dots-Converted White LEDs," *IEEE Transactions on Electron Devices* 66, no. 11 (2019): 4778–4783, https://doi.org/10.1109/ted.2019.2937340.

35. H. Gao, Y. Xie, C. Geng, S. Xu, and W. Bi, "Efficiency Enhancement of Quantum-Dot-Converted LEDs by 0D–2D Hybrid Scatterers," *ACS Photonics* 7, no. 12 (2020): 3430–3439, https://doi.org/10.1021/acsphotonics.0c01240.